

Supplement of Atmos. Chem. Phys., 18, 1879–1894, 2018  
<https://doi.org/10.5194/acp-18-1879-2018-supplement>  
© Author(s) 2018. This work is distributed under  
the Creative Commons Attribution 4.0 License.



*Supplement of*

## **Investigating biomass burning aerosol morphology using a laser imaging nephelometer**

**Katherine M. Manfred et al.**

*Correspondence to:* Katherine M. Manfred ([katherine.manfred@noaa.gov](mailto:katherine.manfred@noaa.gov))

The copyright of individual parts of the supplement might differ from the CC BY 4.0 License.

## Supplementary.

This Supplementary material contains additional information and plots for the interested reader.

5 Figure S1 shows the measured cross-section of a single image (1 s integration time) from the imaging nephelometer compared to a Gaussian fit. The profile corresponds to the  $14^\circ$  scattering angle bin. The measurement was acquired while sampling particle-free, dry air ( $\sim 800$  mbar), and therefore represents only Rayleigh scattering. This figure demonstrates that, in the context of this instrument, the laser beam intensity profile is sufficiently Gaussian in nature.

10 Figure S2 depicts the relative contribution of different signals to the raw measurements. The data have all been summed across each angle bin. The raw data (black line) represent a single measurement of the total aerosol population during Fire A (see Section 4.1). The non-particle contributions are shown in colors and stacked. The Rayleigh scattering and helium correction have been scaled for laser power during the measurement, and the Rayleigh scattering has also been corrected for pressure. We note that a much higher laser power is used when measuring only Rayleigh scattering for calibration measurements. The dark background is predominantly accounted for by the voltage across the CCD; the standard deviation across the pixel array and variation for different acquisition times (100 ms compared to 10 s) accounts for  $< 5\%$  of this signal level. The dark background appears to contribute substantially to the signal here because we have summed the signal across all pixels, including those not exposed to scattering from the laser beam (see Figure 2 in the main manuscript).

20 Figure S3 shows a sample pixel-to-angle calibration curve for the 405 nm laser determined by comparing the pixel associated with the measured maxima and minima with the angles of the phase function maxima and minima predicted by Mie theory for monodisperse PSLs with diameters of 520, 600, and 700 nm.

25 The LAS retrieves aerosol size distributions based on scattered 633 nm light. According to the manufacturer's specifications, the light collecting optics cover the solid angles  $90^\circ \pm 57^\circ$ , excluding  $90^\circ \pm 14.8^\circ$ . This translates to  $33^\circ - 75.2^\circ$  and  $104.8^\circ - 147^\circ$  of the scattering phase function with a maximum azimuthal (out of the plane of the phase function) angle of  $57^\circ$  at  $90^\circ$  scattering angle. This means that, for any given phase function, we can calculate the fraction of scattered light theoretically collected and measured by the LAS detection system. Multiplying this fraction by the integrated scatter in absolute units gives the total scatter measured by the LAS. Since the LAS is calibrated for nominally spherical ammonium sulfate particles, we use Mie theory to determine the total scattered measured per particle for each size bin (99 bins). Then, using the parameterizations of  $k_o$ ,  $D_f$ , and  $a$  from described in Section 3.1, we adjust the magnitude of  $N_p$  (the number of monomers per agglomerate) to match the scatter measured by the LAS for each size bin (based on RDG calculations). Thus, we can approximately correlate LAS size bins with fractal sizes.

Figure S4 shows an Allan-Werle deviation plot for scattering signal integrated over a single angle bin (each  $\sim 0.5^\circ$ ) at several measurement angles. This was determined by continuously imaging the phase function of a clean air sample and removing the Rayleigh scattering component to measure a “zero” phase function. Figure S5 shows the Allan-Werle deviation plot for the total integrated scatter at 405 nm for the TSI integrating nephelometer (red) and laser imaging nephelometer (black). Note that the integrating nephelometer has an acquisition rate of 1 Hz for each channel, while the imaging nephelometer has an average acquisition rate of 0.2 Hz. The integrating nephelometer scattering was scaled from 450 nm (observed) to 405 nm using the measured scattering Ångstrom exponent between 450 and 550 nm. The normal mode of operation for the CRD PAS during these experiments included automatic re-zeroing every six minutes, therefore these data are not included in the Allan-Werle plot; the accuracy of both the absorption and extinction channels is  $\pm 5\%$ . Details of the CRD PAS can be found in Lack et al. (2012).

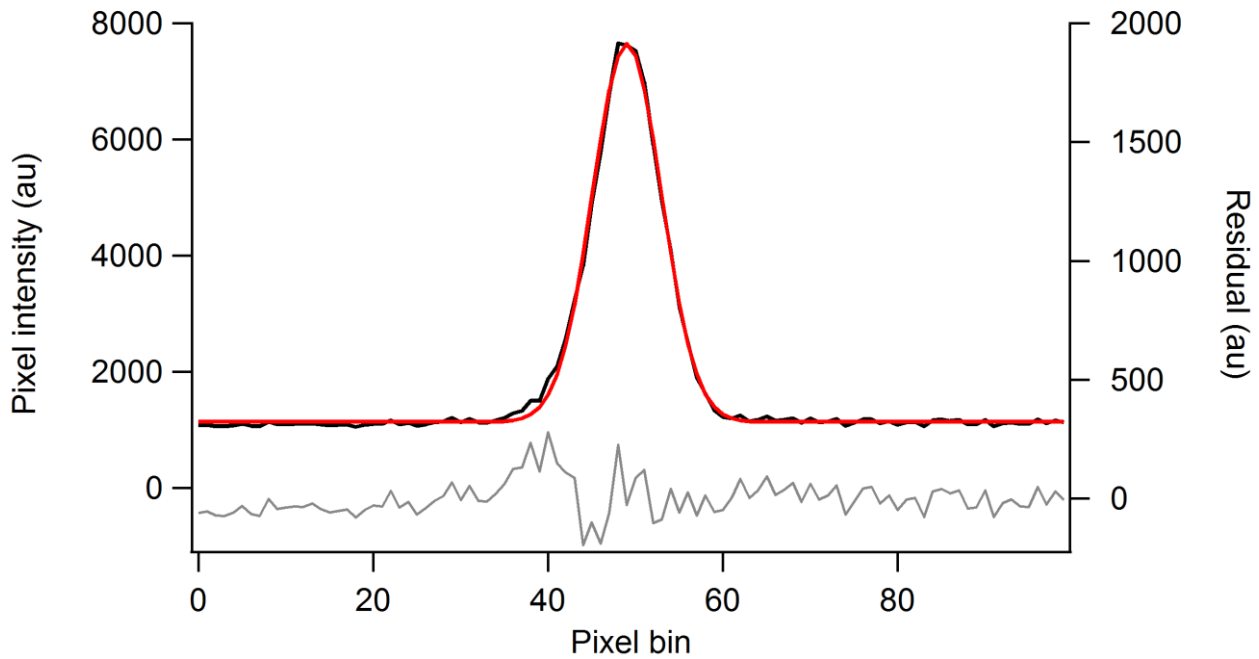
Figure S6 shows a correlation plot for the total integrating aerosol scattering at 405 nm for Fire A. Linear fits are also shown, with the slopes given in the figure caption.

Figure S7 shows a comparison of phase functions modeled using two different fractal parameterizations (RDG model) and four different refractive indices for spherical particles (Mie theory). This plot corresponds to Figure 6(a) in the main manuscript. It is evident that the values used do not significantly alter the general shape of the phase functions, with the RDG model always predicting much more strongly forward-scattering phase functions. Details of the parameterizations, including references, are noted in the caption.

#### References:

- Chakrabarty, R. K., Moosmüller, H., Garro, M. A., Arnott, W. P., Walker, J., Susott, R. A., Babbitt, R. E., Wold, C. E., Lincoln, E. N. and Hao, W. M.: Emissions from the laboratory combustion of wildland fuels: Particle morphology and size, *J. Geophys. Res. Atmos.*, 111(7), 1–16, doi:10.1029/2005JD006659, 2006.
- Chakrabarty, R. K., Moosmüller, H., Chen, L. W. A., Lewis, K., Arnott, W. P., Mazzoleni, C., Dubey, M. K., Wold, C. E., Hao, W. M. and Kreidenweis, S. M.: Brown carbon in tar balls from smoldering biomass combustion, *Atmos. Chem. Phys.*, 10(13), 6363–6370, doi:10.5194/acp-10-6363-2010, 2010.
- Dinar, E., Abo Rziq, A., Spindler, C., Erlick, C., Kiss, G. and Rudich, Y.: The complex refractive index of atmospheric and model humic-like substances (HULIS) retrieved by a cavity ring down aerosol spectrometer (CRD-AS), *Faraday Discuss.*, 137, 279–295, 2008.
- Gwaze, P., Schmid, O., Annegarn, H. J., Andreae, M. O., Huth, J. and Helas, G.: Comparison of three methods of fractal analysis applied to soot aggregates from wood combustion, *J. Aerosol Sci.*, 37(7), 820–838, doi:10.1016/j.jaerosci.2005.06.007, 2006.
- Haynes, W. M., Ed.: *CRC Handbook of Chemistry and Physics*, CRC Press/Taylor & Francis, Boca Raton, FL., 2013.

Lack, D. A., Richardson, M. S., Law, D., Langridge, J. M., Cappa, C. D., McLaughlin, R. J. and Murphy, D. M.: Aircraft instrument for comprehensive characterization of aerosol optical properties, Part 2: Black and brown carbon absorption and absorption enhancement measured with photo acoustic spectroscopy, *Aerosol Sci. Technol.*, 46(5), 555–568, doi:10.1080/02786826.2011.645955, 2012.



**Figure S1:** Measured pixel intensity across the  $14^\circ$  scattering angle bin (black) is shown compared with Gaussian fit (red) for a single CCD image (1 sec integration time) when the imaging nephelometer is filled with filtered air and signal arises solely from Rayleigh scattering. The residual (grey) demonstrates the quality of the fit.

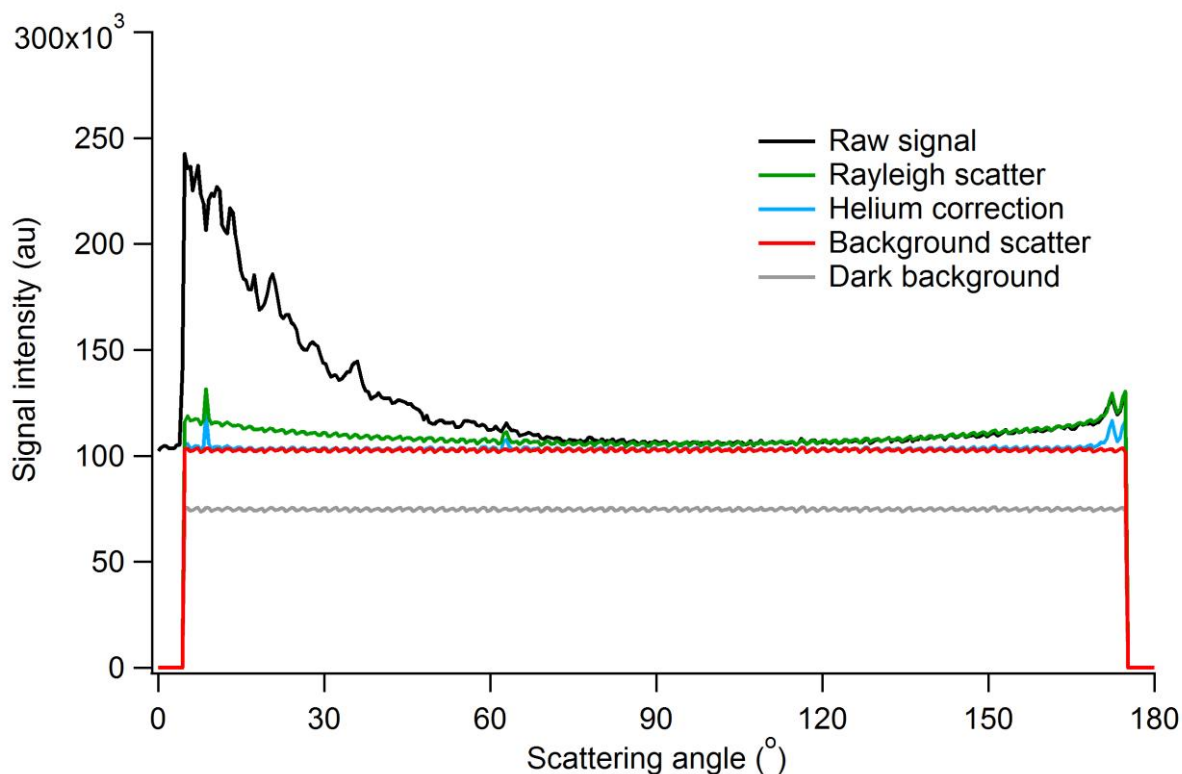


Figure S2: Contribution of various sources of signal to a single measurement of scattering of the total aerosol population (bypass channel) during Fire A. The black line indicates the raw signal summed across all pixels for each angle bin. The coloured lines show the corrections applied, and are stacked in the following order: dark background (grey), background scatter (likely caused by temperature variations of the CCD and multiple scatter from the walls), helium correction (direct wall scatter), and Rayleigh contribution. The dark background is dominated by the signal associated with the voltage across the CCD; read-out and single-shot thermal noise together account for <5%. The Rayleigh and helium corrections have been corrected for laser power, and the Rayleigh contribution has also been corrected for pressure. The integrated scatter from the aerosol particles was measured to be 88.3 Mm<sup>-1</sup> in the instrument corresponding to 4741 Mm<sup>-1</sup> in the original sample after accounting for dilution.

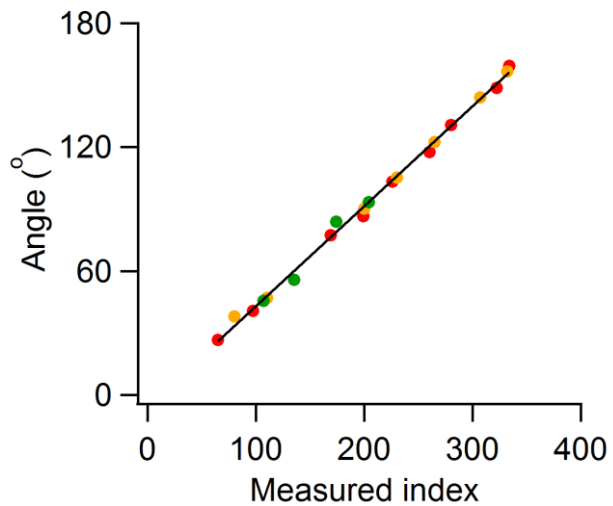


Figure S3: Pixel-to-angle calibration plot for 405 nm showing angles (calculated using Mie theory) versus measured indices for maxima and minima appearing in phase functions for monodisperse PSL: 520 nm (green), 600nm (orange), and 700 nm (red). The fit, including all sizes, has a slope of 0.484, intercept of -5.45, and  $R^2$  value of 0.997.

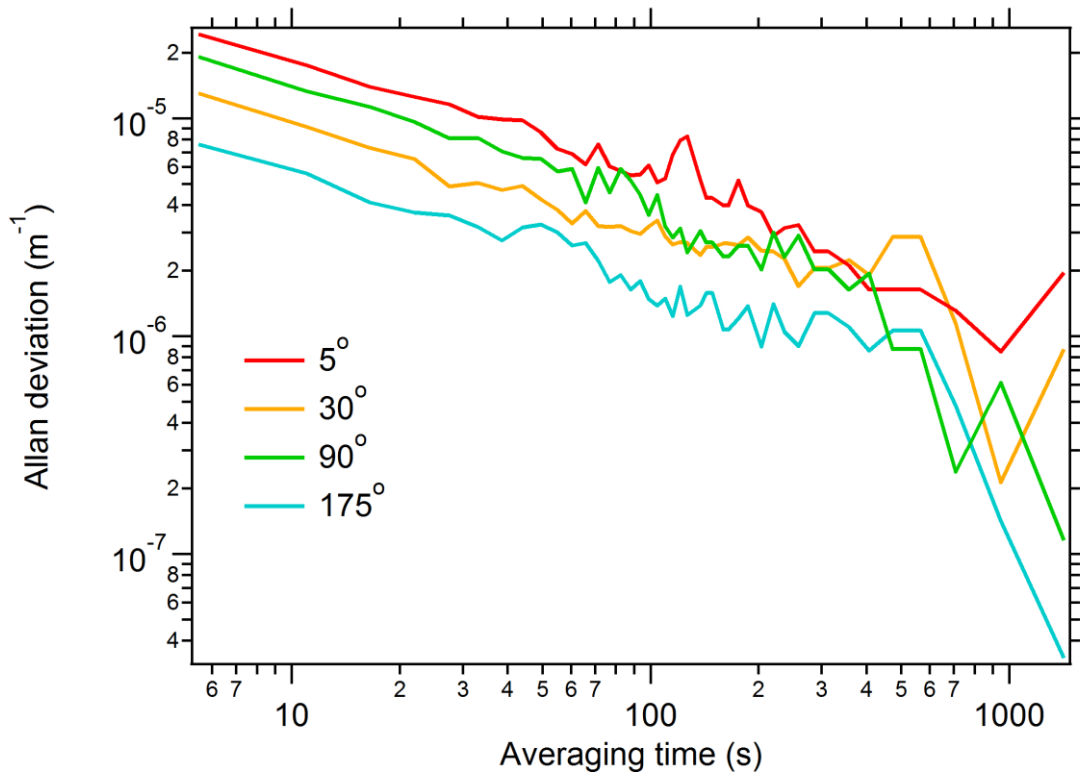


Figure S4: Allan-Werle deviation plot for individual scattering angle bins (each  $\sim 0.5^\circ$  bin size). Data collected for particle-free air (Rayleigh scattering contribution removed).

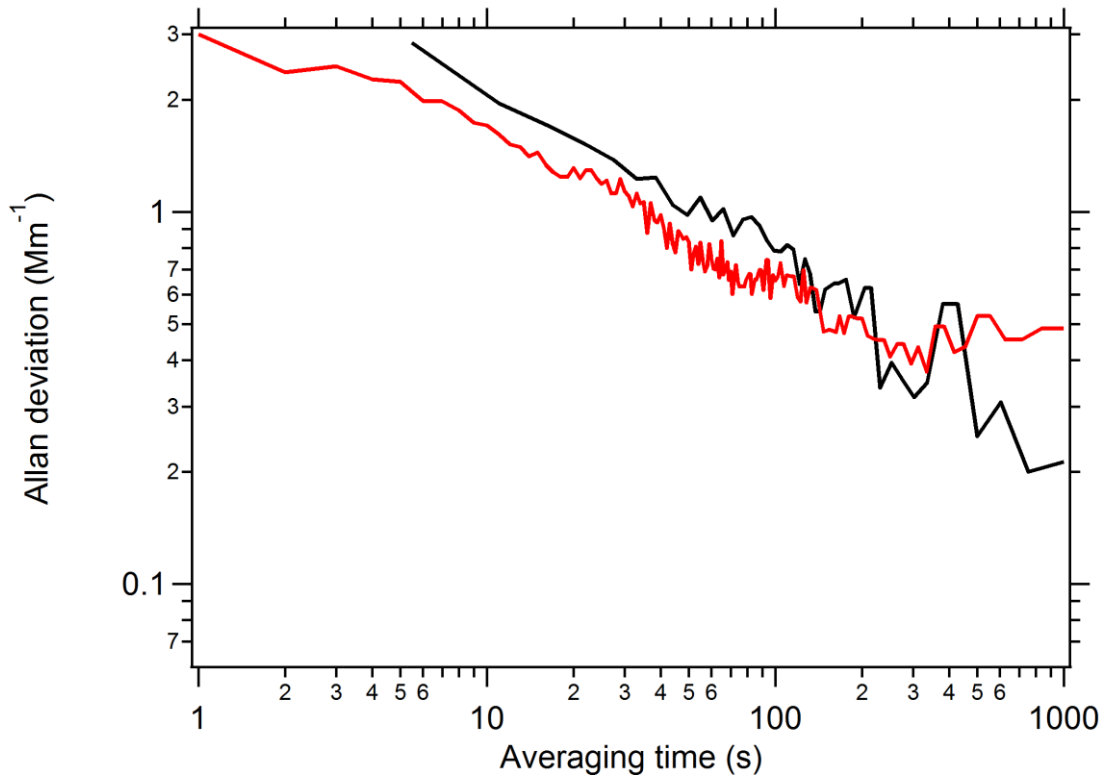


Figure S5: Allan-Werle deviation plot of integrated scatter at 405 nm for the imaging nephelometer (black) and integrating nephelometer (red). The integrating nephelometer measurements at 450 nm were scaled to 405 nm using the measured scattering Ångstrom exponent between 450 and 550 nm. Instruments were co-sampling filtered air.

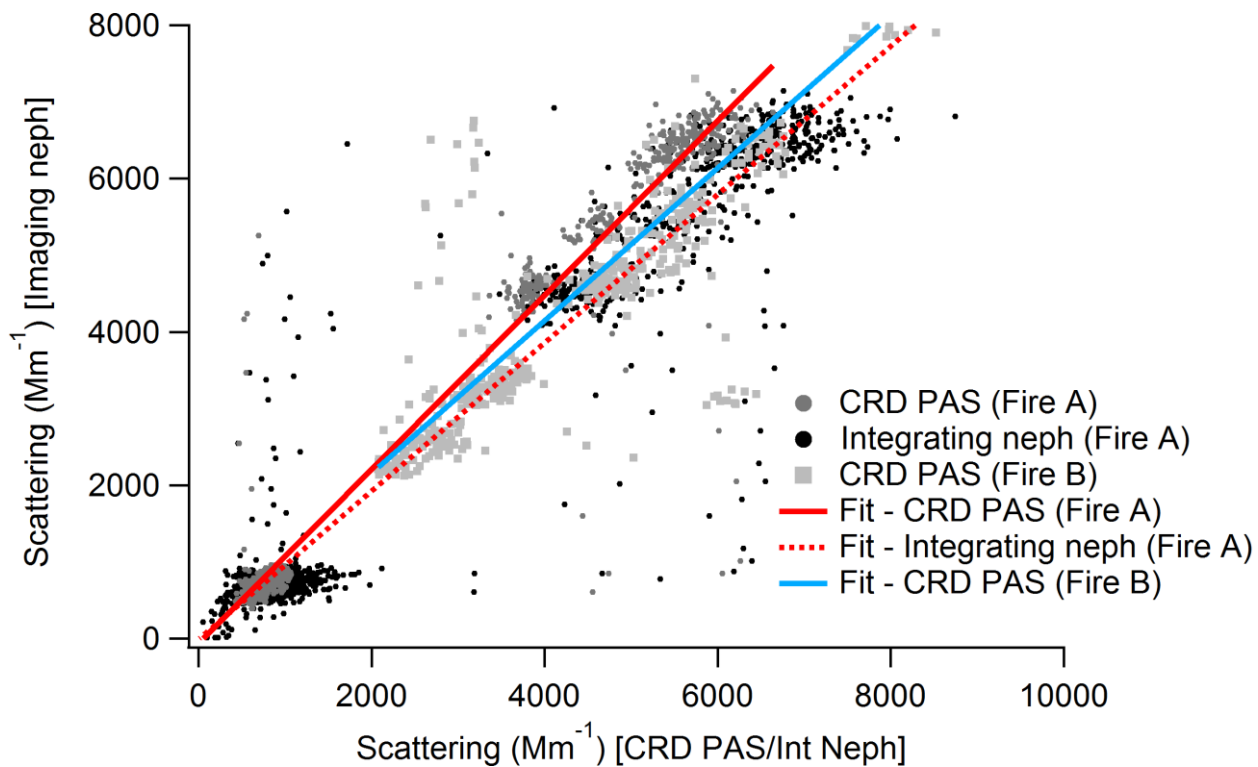
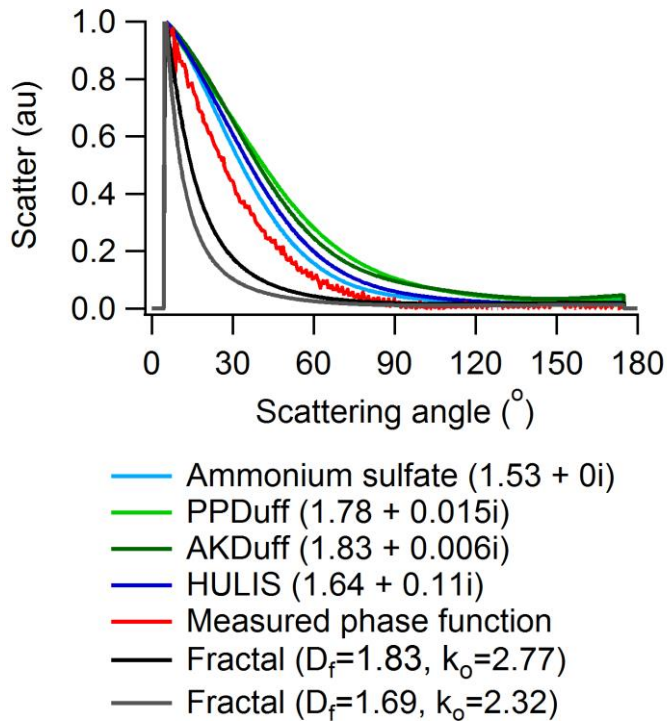


Figure S6: Correlation plot of integrated scattering at 405 nm for Fire A (circles) and Fire B (triangles). The slope for the imaging nephelometer measurements vs CRD PAS measurements is 1.137 for Fire A (grey dots, solid red line) and 0.967 for Fire B (open triangles, solid blue line). The slope for the imaging nephelometer measurements vs integrating nephelometer measurements (black dots, dashed red line) is 0.996.

5



5 **Figure S7: Intercomparison of measured and modelled phase functions using different parameterizations for Fire A (bypass channel) at 405 nm: measured (red); Mie theory using refractive index for ammonium sulfate (light blue) (Haynes, 2013), ponderosa pine duff (PPDuff; light green) (Chakrabarty et al., 2010), Alaskan duff (AKDuff; dark green) (Chakrabarty et al., 2010), and humic-like substances (dark blue) (Dinar et al., 2008); RDG theory using fractal parameterization for ponderosa pine (grey) (Chakrabarty et al., 2006) and beech (black) (Gwaze et al., 2006). All curves were normalized to unity at  $5^{\circ}$  scattering angle.**